UPSCALING OF SMA FILM-BASED ELASTOCALORIC COOLING

Giulia Ulpiani[*1], Florian Bruederlin[2], Raphael Weidemann[2], Gianluca Ranzi[1], Mat Santamouris[3], Manfred Kohl[2]

[1] School of Civil Engineering, The University of Sydney, Sydney, New South Wales, Australia.
[2] Institute of Microstructure Technology, Karlsruhe Institute of Technology (KIT), Karlsruhe, Germany
[3] Faculty of Built Environment, University of New South Wales, Sydney, New South Wales, Australia

[*]Corresponding Author
Address: School of Civil Engineering Room 260, Building J05, 225 Shepherd St, Darlington NSW 2006
Email address: giulia.ulpiani@sydney.edu.au
Phone number: +61481600997

Abstract
A new concept of upscaling a shape memory alloy (SMA) film based elastocaloric cooling device is presented by arranging SMA films in parallel to increase the specific cooling capacity at low actuation force, while maintaining the large surface-to-volume ratio needed for rapid heat transfer. Selected materials are cold-rolled TiNiFe films that exhibit maximum adiabatic temperature changes of 27.3 and -18.1 K upon loading and unloading, respectively. Demonstrators are designed, fabricated and characterized consisting of five free-standing TiNiFe film bridges that are coupled antagonistically for work recovery. Thermomechanical cycling is performed by out-of-plane deflection of the SMA bridges, while heat transfer is established through mechanical contact with solid heat sink/source elements. The cooling capacity of the demonstrators scales with the number of active SMA films, which confirms the concept of parallelization for upscaling. Investigated demonstrators reach a maximum cooling capacity of about 900 mW compared to a maximum of about 200 mW achieved for reference devices consisting of a single TiNiFe film. The investigation also reveals a number of open issues related to narrow fabrication tolerances upon upscaling, which may cause different plastic straining and varying inhomogeneous stress accumulation among the individual SMA films.

Keywords
Solid state cooling; Elastocaloric effect; Shape memory alloys; Superelastic films; Parallelization for upscaling; Thermo-mechanical coupling

1. Introduction
The growing need for efficient, environmentally friendly refrigeration leads to an increased demand for innovative, eco-friendly cooling technologies. Ferroic solid-state cooling based on caloric effects is among the most promising candidates, as they do not rely on refrigerants contributing to global warming [1]. Especially elastocaloric cooling stands out as the caloric technology having the highest potential to replace environmentally harmful vapor compression and energy-inefficient thermoelectrics [2]. Elastocaloric cooling is based on a reversible stress-

induced martensitic phase transformation. Large elastocaloric effects have been observed, e.g., in copper-based shape memory alloys (SMAs) showing temperature changes ΔT up to 15 K [3] and in TiNi based alloys reaching ΔT up to 40 K [4,5].

The elastocaloric behavior depends on a martensitic transformation occurring at atomic scale that affects the coupled mechanical and thermal performance at larger scales up to the macro scale. Austenite exists at high temperature and low stress and features a cubic crystal structure with high crystallographic symmetry, whereas martensite is metastable at low temperature and high stress and has a lower crystallographic symmetry [6,7]. When the material in austenitic state is uniaxially loaded above a certain critical stress, the phase transformation occurs exothermically. Heat is either released to the surroundings at low strain rates and thus under quasi-isothermal conditions or it causes an increase of the material's temperature at high strain rates near adiabatic conditions. Reportedly, elastocaloric cooling has the potential to achieve material level efficiencies in the order of 80% of the thermodynamic maximum (Carnot efficiency) [8], which is about 20% higher than that reached by vapor-compression systems.

Despite the encouraging perspective, it remains a fairly underexplored technology. To be suitable for the cooling sector, an elastocaloric material has to meet several critical requirements including large latent heat of phase transformation, high adiabatic temperature change at the intended operating temperature, high fatigue resistance, low heat capacity and high thermal conductivity, whilst being easily manufacturable [9–11]. Recently, several macro-scale demonstrators have been developed by making use of TiNi wires [12,13], TiNi tubes [14] and plates [15,16], and by considering different layouts and modes of operation. Among the few demonstrators realized, the maximum experimentally measured COP for heating (quotient of released heat and applied work) of 7 at the macroscale refers to a demonstrator based on active regeneration [15]. The use of SMA films and foils has the advantage to enable rapid heat transfer due to their large surface-to-volume ratio, which is particularly attractive for miniature scale applications [10,17,18]. At the miniature scale, cooling demonstrators based on SMA films using contact heat transfer show a COP upon cooling (quotient of absorbed heat and applied work) of up to 6.7 and high specific cooling power (nearly 19 W/g) [18], while requiring comparatively low actuation forces [19].

The maximum cooling capacity is limited by the latent heat of the film undergoing stress-induced phase transformation, film mass and cycling frequency. Test devices based on a single SMA film of 30 μm thickness reveal maximum values of cooling capacity of 200 mW [18]. While this power level might be suitable for thermal control at the micro scale, upscaling will be essential to meet the demands of cooling applications at larger scales. Therefore, we propose the new concept of upscaling by arranging SMA films in parallel to increase the overall film mass, while maintaining the large surface-to-volume ratio needed for rapid heat transfer and high specific cooling capacity. Thus, the motivation of this investigation is to explore how film-based elastocaloric cooling can be tuned for different application-specific dimensions. Parallelization makes use of the high specific cooling capacity, fast heat transfer and low actuation forces typical for film-based elastocaloric cooling.

2. Material properties

Superelastic $Ti_{50.5}Ni_{49.1}Fe_{0.4}$, films are prepared by cold-rolling with two thicknesses of 30 and 40 μm for materials testing. For convenience, these materials will be denoted as SMA films in the following. Final heat treatment is performed at 500 °C for 30 min. For the lateral dimensions the films are mechanically cut in rolling direction taking into account the texture dependency of the elastocaloric effect in the material [19,20].

Mechanical characterization is performed by tensile testing. During tensile loading and unloading, the surface temperature distribution of the SMA film is recorded by infrared thermography. Therefore, specimens are coated with a graphite spray to homogenize the emissivity at about 0.95. All tests are conducted at ambient temperature. After initial training to stabilize the material behavior, samples are tested at strain rates from 10^{-4} to 1 s^{-1} in strain-control mode. Regardless of the strain rate, a 10 s holding time is allowed between loading and unloading and between each cycle for thermal equalization with the surroundings.

Figure 1 a) shows superelastic stress-strain characteristics of the material for different strain rates (dotted lines). At very low rate of 10^{-4} s^{-1}, the heat exchange with the environment dominates resulting in quasi-isothermal conditions. In this case, the critical stress of forward and reverse transformation are determined to be σ_{crit}^{A-M} =419.8 MPa and σ_{crit}^{M-A} =205.6 MPa, respectively. Assuming work recovery, the work input needed to drive the SMA material through the full loading cycle is represented by the area enclosed by the loading and unloading path in the stress strain diagram, which is 10 MJ/m³ at the given strain rate. The input work increases with the strain rate due to the self-heating and -cooling effect by 110 % in the given range.

Figure 1 b) shows the strain rate-dependence of maximum and minimum temperature as well as of the input work. Experimental data are overlapped in the form of an error bar to account for the slight variations recorded over different cycles. When strain rates are increased, the latent heat of the phase transformation cannot be released completely to the ambient causing self-heating upon loading and self-cooling upon unloading. A saturation of the temperature change for increasing strain rate occurs at about 0.3 s^{-1} in agreement with [21], reflecting the adiabatic limit, above which heat exchange of the specimen with the ambient can be neglected. Adiabatic temperature changes of 27.3 K for heating and of -18.1 K for cooling are reached. Similar heating/cooling asymmetries are observed in literature, e.g. on cold-drawn TiNi wires [22]. Figure 1 c) illustrates the temperature evolution of the SMA foil during one load cycle at a strain rate of 1 s^{-1}. The stress induced transformation from austenite to martensite during loading leads to a steep increase of temperature. During the holding time of 10 s the temperature reduces to ambient. Subsequent unloading leads to the reverse phase transformation, heat absorption and a corresponding temperature drop. Figure 1 d) shows corresponding surface temperature profiles of the specimen at distinct times in the elastocaloric cycle. The observed inhomogeneities in temperature profiles correlate with inhomogeneities in strain profiles. In particular, digital image correlation measurements reveal formation and propagation of Lüder's like bands that increase in number for increasing strain rate resulting in a fairly homogeneous temperature profile in the adiabatic limit. A detailed investigation of the strain-rate dependent non-local transformation behavior of the SMA film specimens can be found in [23], where mesoscale simulations predict the correlated mechanical and thermal local response of the films including band formation and evolution, tilt angle as well as strain-rate dependence. At the macro scale, further inhomogeneities may occur, e.g., due to non-uniform loading or fabrication tolerances.

In this study, the macroscale material behavior is simulated using the finite element method based on a 3D Tanaka-type phenomenological model assuming material isotropy and two-phase transformation between high temperature austenitic and low temperature martensitic phase (see Appendix). The simulation of a load cycle starts from a fully austenitic stress-free state. At the end of each cycle, the stress-strain and thermal profiles are determined. The integrals of the loading and unloading characteristics are computed and subtracted to obtain the non-recoverable work input. The simulation results are plotted in Figure 1 a-c) alongside with the experimental results.

The efficiency of the elastocaloric performance of the SMA at the material level can be determined by the material coefficient of performance. For heating and cooling, it is calculated as follows:

$$COP_{mat} = \frac{\rho \cdot c_p \cdot \Delta T_{ad}}{\Delta W_{input}}.$$ (1)

The product of specific heat capacity and measured adiabatic temperature change $c_p \cdot \Delta T_{ad}$ in Eq.1 estimates the released (absorbed) latent heat. The investigated SMA films show a specific latent heat of 12.3 J/g for the exothermic forward transition from austenite to martensite and 8.2 J/g for the endothermic reverse transition. The input work (ΔW_{input}) is determined from the hysteresis of the stress-strain characteristics as displayed in Figure 1 a) by numerical integration. Thereby, we assume complete work recovery upon unloading. Mechanical hysteresis (input work) and latent heat are saturating for increasing strain rate in the considered range (Figures 1 a-b). At adiabatic conditions, the material coefficient of performance for heating ($COP_{mat,h}$) reaches 3.8.
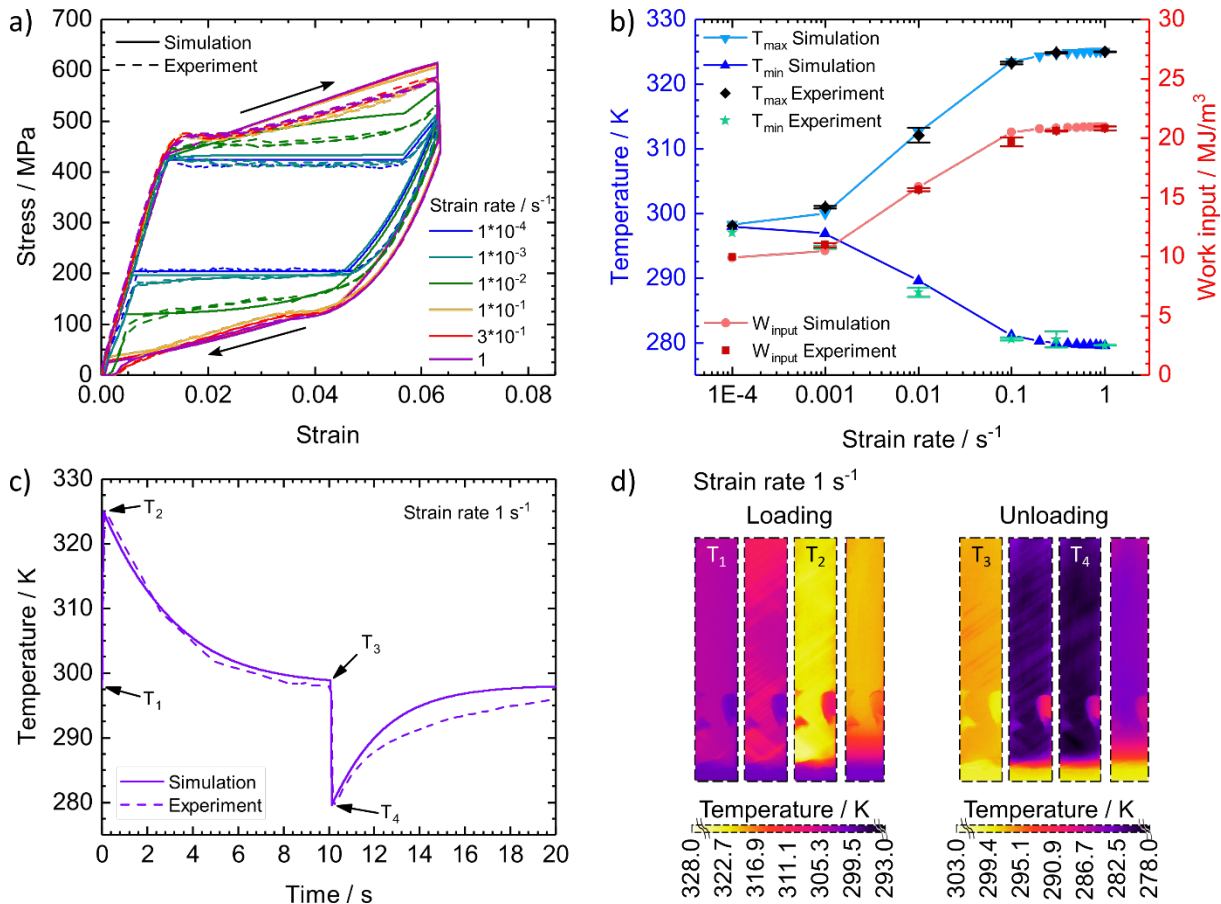
Figure 1: Experimental and simulation results for the 40 μm thick TiNiFe films: a) stress-strain characteristics at various strain rates, b) semi-logarithmic plot of temperature and work input versus strain rate, c) time-resolved evolution of average temperature under adiabatic conditions, d) IR thermographs recorded during loading and unloading at a time interval of 0.25 s. Average temperatures T1/T3 and T2/T4 correspond to the beginning and end of loading/unloading, respectively.

3. **Concept of upscaling**

The current developments in film-based elastocaloric devices mark pivotal steps towards the realization of innovative cooling and heat pumping systems for applications at the miniature scale. Upscaling of SMA film-based devices may lead to distributed cooling systems that pave the way for applications at larger scales.

In the following, the concept and operation principle of the demonstrators for upscaling are presented and include five SMA films arranged in parallel. The number of films has been limited by the available actuator for loading. Figures 2 a) and b) show a schematic of the demonstrator compared to the concept of a single SMA bridge device developed previously [18]. The overall film mass is increased by arranging the films in a parallel configuration of SMA bridges. In this approach, the thickness of SMA films is not changed to maintain the large surface-to-volume ratio needed for rapid heat transfer. Freestanding SMA films are supported by a holding frame on both ends. They are loaded by out-of-plane deflection using the concept of solid-to-solid heat transfer similar to the concept of single SMA bridge device [19,24]. As shown in Figure 2 b), the heat sink elements have a functional surface on both sides, so that heat transfer occurs twice within a single operation cycle with two different SMA films. All heat sink and source elements are connected in the third dimension that is not displayed in the schematic. Through the thermal connection of sink and source elements the heating and cooling capacities of the single films are interconnected in a parallel manner, respectively, and thus add up.
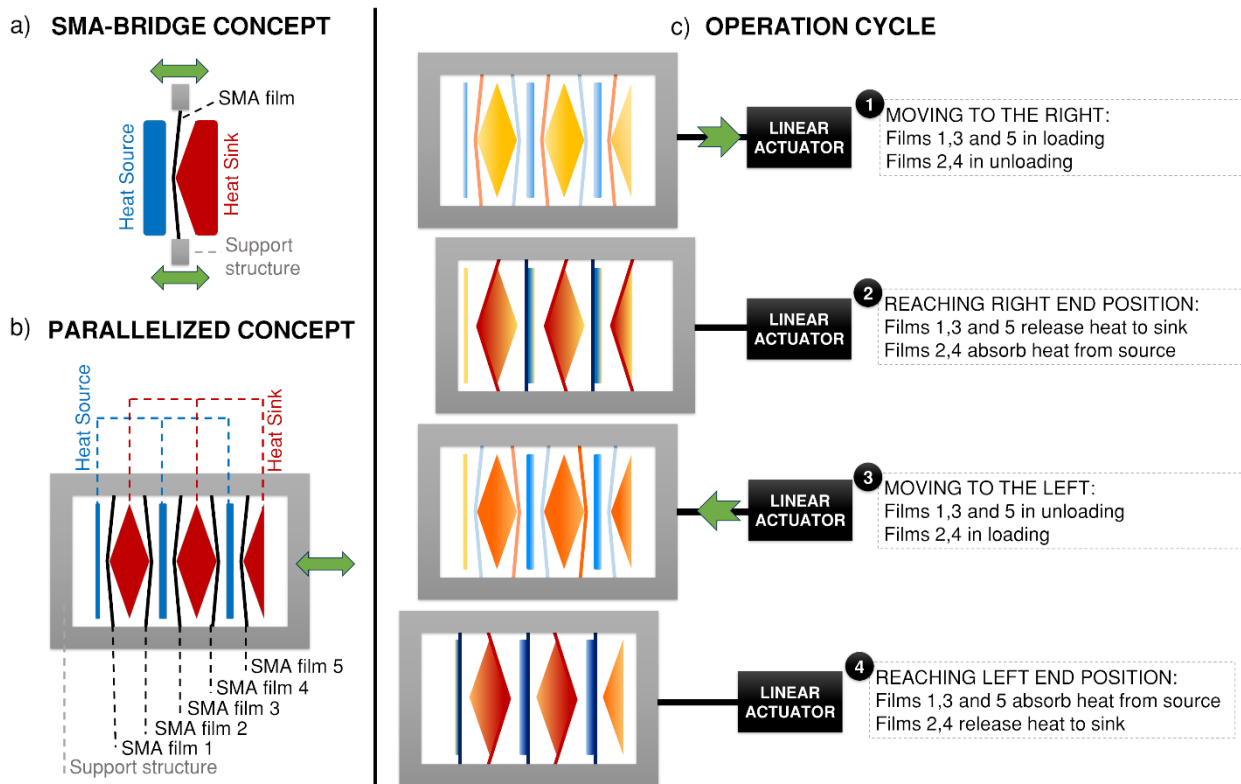

Figure 2: Schematic of the parallelized design and of operation cycle: a) design concept of single SMA bridge device, b) proposed design modifications to operate five SMA films in parallel, c) typical operation cycle and role of the actuator.

The operation cycle of the parallelized setup is displayed in Figure 2 c). The cycle starts from the position displayed in step 1 with slightly pre-strained SMA films at half-way position between

sink and source elements. As the linear actuator moves the support structure to the right (step 1), three films are pressed against the diamond-shaped heat sink elements and generate heat upon loading. The diamond shaped heat sink has no sharp edges but it is rounded to about 1 mm in radius at the tip. As the bending radius is large compared to the film thickness, tensile strain given by the cone angle of heat sink is dominating, while bending strain is negligible in the present case of deflection loading of the films. During full contact between film and heat sink (end point of loading), frictional forces become important. In this case, the assumption of dominating tensile strain is no longer valid, but also irrelevant as this is the point at which the transformation is completed and heat transfer occurs. Compared to pure tension, the force to be applied can thus be reduced considerably [19,24]. The other two films release stress and cool down while contacting the nearly flat heat source elements. These steps occur simultaneously as the result of the same mechanical action, requiring only a single linear actuator. At the right end position (step 2) the films reach maximum and minimum stress respectively. After a specified holding time for the heat transfer, the actuator inverts its motion (step 3) so that loaded films progressively relax, while relaxed ones become loaded. At the left end (step 4) three SMA films are held in contact with the heat source elements and two SMA films are held against the heat sink elements for as much time as during step 2. The temperature lift between source and sink elements increments at each cycle until a steady-state condition with the ambient is established. In the setup, loading and unloading of films always occurs side by side. The pre-straining and antagonistic coupling of the films ensures that the work released during unloading of SMA films is used to help loading their antagonistic partners and, thus, to recover work. In the present case, work recovery is incomplete due to the following issues: (i) the force-displacement characteristics are distorted as the films are deflected in out-of-plane direction and (ii) the asymmetry in number of SMA films causes a different force required for the two opposing loading directions.

4. Demonstrator layout and fabrication
The layout of the demonstrator is illustrated in Figure 3 a). It comprises the following components: i) SMA module consisting of TiNiFe films and holding frame, ii) heat sink and source elements including auxiliary components for thermal insulation and mechanical connection, iii) actuator module including the linear actuator and its control system as well as iv) a number of thermal sensors.

In the following, two technological variants (demonstrator 1 and 2) will be presented that slightly differ with respect to the mass of the heat source elements and the method of bonding the SMA films using an adaptive holding frame.
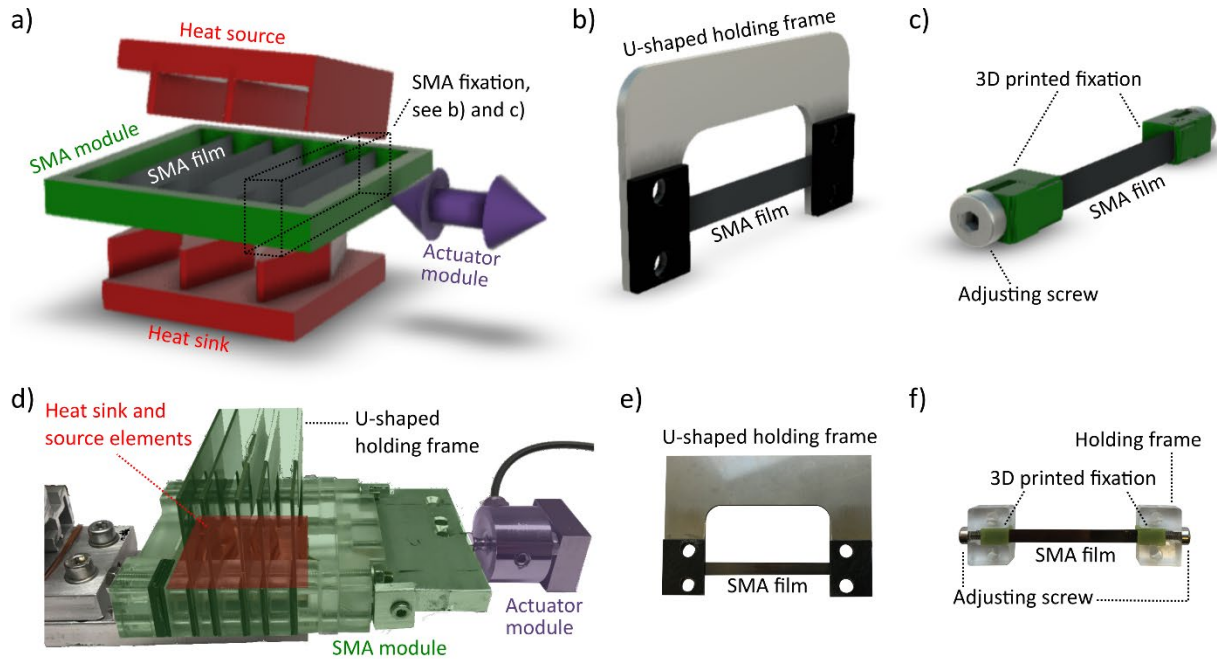
Figure 3: (a) 3D schematic layout showing the major components of the demonstrators: SMA module consisting of SMA films and holding frame, heat sink and source elements and the actuator module; (b) 3D schematic of the U-shaped holding frame used to bond the SMA films in demonstrator 1; (c) 3D schematic of the 3D printed fixations used to bond the SMA films in demonstrator 2; (d) built demonstrator 1; (e) built U-shaped holding frame (demonstrator 1); (f) built 3D printed fixations (demonstrator 2).

SMA films of 30 μm thickness are used for demonstrator fabrication. The SMA films are laser cut in stripes with lateral dimensions of 56 x 4 mm². Their edges are mechanically polished to remove imperfections. Then in case of demonstrator 1 (Figure 3, d), the SMA films are bonded to U-shaped holding frames made from steel. In this way, the ends are fixed and no additional stress components arise due to potential tilting (compare Figure 3, b and e). To improve the bonding strength and act more gently on the SMA films, these are glued to hard paper plates by using a two-component epoxy adhesive. Alternatively, in demonstrator 2, the SMA films are bonded onto separate 3D printed fixations inserted into a common holding frame that is connected to the actuation unit (compare Figure 3, c and f). The back screw is used to adjust the initial strain of each film, independently of the others. The distances between the SMA films are precisely adjusted by means of spacer elements.

Both heat sink and source elements are precision milled from copper and their contact surfaces are mechanically polished to optimize heat transfer and to avoid stress peaks. The diamond-shape of the heat sink elements is designed to impart a maximum strain of 4.7 % on the SMA foils. The heat source elements are designed comparatively flat, yet slightly cambered at an angle of < 1° to achieve good surface contact. Thermal decoupling between source and sink elements is achieved by several means including 1 mm thick PMMA insulation layers with thermal conductivity of 0.19 W/mK. Parasitic heat transfer between the heat source elements and the supporting aluminum base plate is mitigated by connecting them with four glass fiber reinforced polyamide screws and by integrating an intermediate 5 mm thick PMMA spacer with 2 mm deep honeycomb pits on the

contact surface. The mass of heat sink and source are 79.8 and 22.7 g, respectively, in case of demonstrator 1 and 79.8 and 62.1 g, respectively, in case of demonstrator 2.

The actuator module operates the demonstrator devices by alternating motion of the SMA module using a single ironless synchronous linear actuator. The actuator is operated by means of position-controlled motion profiles coded in LabVIEW. Sinusoidal loading/unloading tracts are combined with constant holding phases at the end positions of the sine curve with duration equal to a quarter of the cycle period such that each of the four steps of the cycle are equally distributed in time.

The system performance during operation is monitored by six temperature sensors. Three sensors are used to measure the external surface temperature of the heat sink and source and as much are placed inside the diamond-shaped elements in contact with the SMA, at mid-depth. In addition, the force applied to the SMA unit is recorded by a load cell with nominal force of 500 N and the internal position sensing of the actuator is monitored as well. The assembly of the demonstrator is challenging as tolerances may accumulate and affect the overall system performance. Provided that these challenges are appropriately met, an upscaled version of the presented setup (flat external surfaces, static heat reservoirs with dynamic moving rack in between containing the SMA films) could be devised for integration into panels, e.g. for the building sector [9].

5. Demonstrator performance

Figures 4 a) and b) show the time-resolved displacement of the SMA module and the corresponding force for one operation cycle at a frequency of 1 Hz in demonstrator 1. The motor follows a sinusoidal track with holding times at the turning points to maintain the contact for heat transfer. Figure 4 c) shows the force-displacement characteristic, which is not symmetric, since an uneven number of SMA films is utilized. The course of the force-displacement characteristic reflects the superelastic performance of the SMA material (for comparison see Figure 1 a), as well as the afore-mentioned distortion due to the out-of-plane deflection and the preloading/prestraining of antagonistic films.
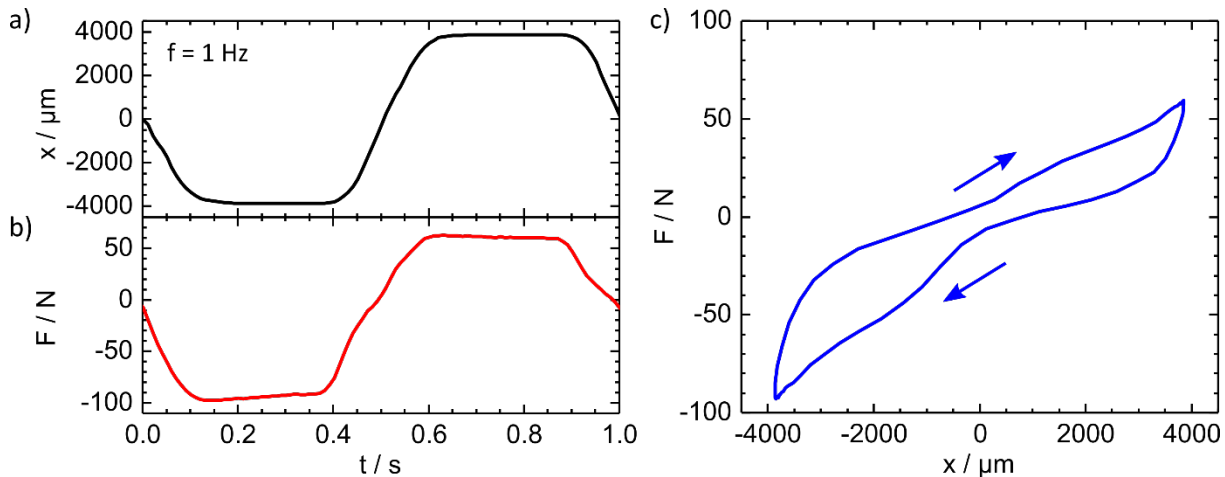

Figure 4: Time-resolved displacement x of the SMA module (a) and corresponding force F (b) during one operation cycle at 1 Hz illustrating the sinusoidal movement and holding times at the turning points. (c) Typical force-displacement characteristic revealing the superplastic performance of the SMA films. The uneven number of films causes an asymmetry: Two SMA films are maximally strained at the right turning point and three SMA films are maximally strained at the left turning point. The antagonistic performance enables work recovery.

The temperature evolution of heat sink and source of demonstrators 1 and 2 is shown in Figure 5 during the first 100 s at the operation frequency of 1 Hz. Heat sink and source elements have an almost uniform temperature. Therefore, temperature sensors placed inside the heat sink and source elements next to the SMA films reveal a consistent temperature evolution regardless of their exact location. Heat is transferred from the heat source to the heat sink stepwise in each cycle by the SMA films. As a result, the heat source cools down, while the heat sink heats up. After a sufficiently large number of cycles, saturation occurs due to competing heat transfer effects [10]. The heat source changes its temperature faster compared to the sink, since its thermal mass is lower.
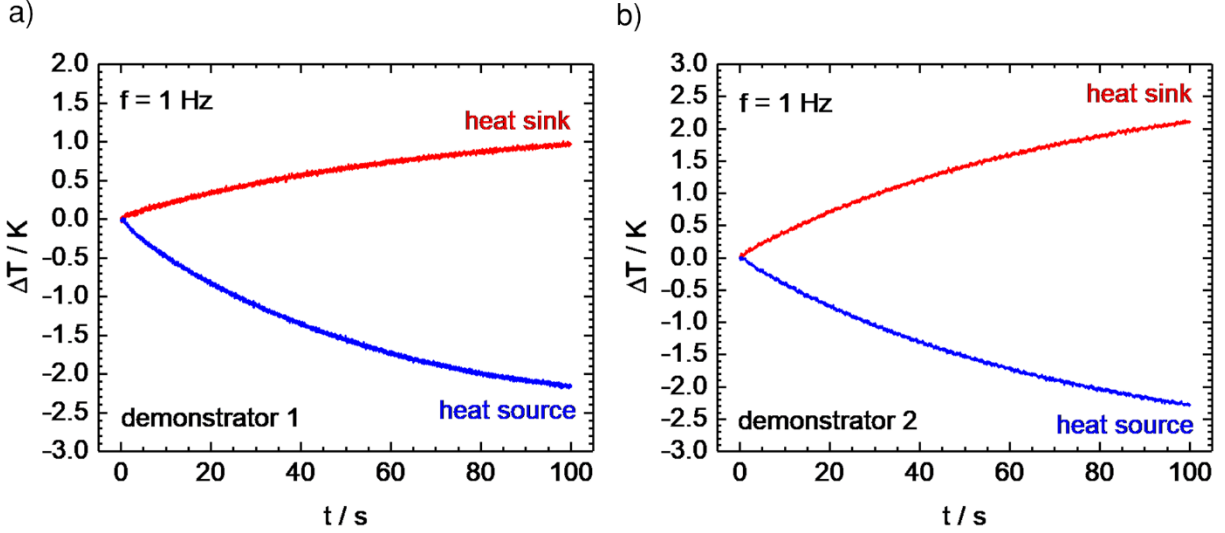

Figure 5: Time-dependent temperature evolution of heat sink and source of demonstrator 1 (a) and 2 (b) at 1 Hz.

Within the initial 100 s, the temperature changes of heat sink and source $\Delta T_h / \Delta T_c$ are about 0.9/ 2.1 K for demonstrator 1 and 2.1/2.3 K for demonstrator 2. These temperature changes are smaller compared to single SMA film devices indicating that heat transfer between parallelized SMA films and heat source elements is reduced and parasitic heat losses are enhanced. Additionally, steady state conditions are not reached after the shown 100 s of operation. As the thermal masses of heat sink and source elements are known, the cooling power at zero temperature span $\dot{Q}_0^{cool}$ can be derived from the initial 10 s temperature evolution of these elements after elastocaloric cycling is started:

$$\dot{Q}_0^{cool} = m_{source} c_p \dot{T}_{source} \tag{2}$$

where m_{source} is the mass of the heat source element, c_p the specific heat capacity of the source taken at 385 J/kgK and $\dot{T}_{source}$ the initial rate of the temperature change. This method gives an upper limit for the cooling power.

Figures 6 a) and b) display the frequency dependence of specific cooling capacity and corresponding COP values for both demonstrator devices, respectively. The specific cooling capacity exhibits a strong increase for increasing operation frequency similar to single SMA film devices, which exhibit optimum performance at 4 Hz [18]. Due to experimental reasons, however, the maximum frequency of 2 Hz could only be reached for demonstrator 1. At operation frequency

of 1 Hz, $\dot{Q}_0^{cool}$ is determined to be 0.35 and 0.9 W for demonstrators 1 and 2, respectively. The values of cooling capacity are considerably larger compared to single SMA film devices, which confirms the benefit of the concept of parallelization for upscaling. The corresponding values of specific cooling capacity normalized to the mass of active SMA films $\dot{q}_0^{cool}$ are 2.25 and 4.67 W/g, respectively. The obtained results are summarized in Table 1. The input work of the demonstrators is defined by numerical integration of experimental force-displacement data. The corresponding COP values are determined by the ratio of cooling capacity and mechanical work per cycle. COP values show a rather large scatter, as reproducibility is limited by accumulation of plastic deformation being different for each SMA film. This issue will be discussed below in more detail. Within the experimental uncertainty, the COP values are almost independent of the operation frequency, i.e., the cooling capacity increases to the same extent as the mechanical work input does. The COP values of demonstrator 2 are higher compared to demonstrator 1, which is attributed to the improved method of bonding the SMA films using an adaptive holding frame. This results in a better thermal contact between SMA films and heat source and, thus, improved heat transfer. Furthermore, loading is more homogeneous, which causes a more uniform phase transformation.
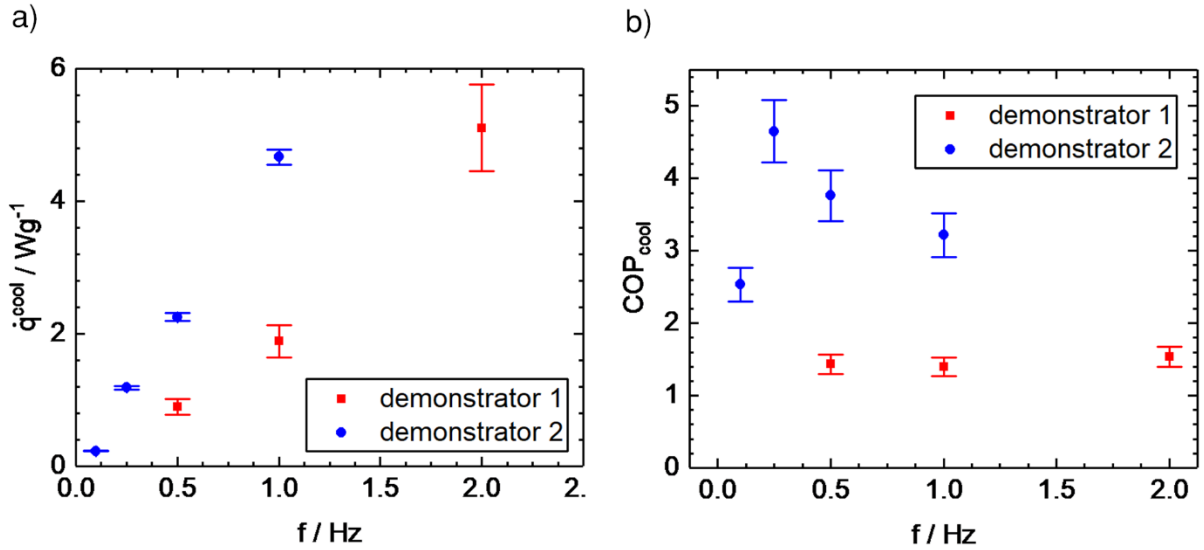

Figure 6: Frequency (f) dependence of specific cooling capacity (a) and cooling COP (b) of demonstrator devices 1 and 2.

6. Discussion

The large caloric effect and surface-to-volume ratio of TiNi-based films are promising for high specific cooling capacity and high operation frequencies. Parallelization, in turn, should enable the increase of cooling capacity paving the way for applications at length scales beyond the micro scale. Previous work on SMA film-based cooling mainly addressed the design and performance of various single film devices as well as the enhancement of temperature change by cascading [25]. In order to address the topic of upscaling by parallelization of SMA films, the following key issues need to be evaluated:

(i) Increase of cooling capacity is the main motivation of this investigation. By increasing the number of films through parallelization, the absolute cooling capacity should increase accordingly.

(ii) Heat transfer should be as efficient as for single SMA film devices. Despite parallelization, the specific cooling capacity should not change for increasing number of SMA films.

(iii) Heat transfer at the heat sink and source elements should be reproducible.

(iv) A high reliability during elastocaloric cycling is essential. Fatigue life of the demonstrator devices should be comparable to the fatigue life of single film devices and ideally reach the fatigue life observed in tensile experiments.

Table 1 summarizes the main results on demonstrators 1 and 2, consisting of five parallel free-standing TiNiFe films, compared to previous results on single SMA film devices. In addition, the performance of selected elastocaloric cooling demonstrators based on fluidic heat transfer is included for comparison.

Table 1 *Absolute and specific cooling capacities achieved for demonstrators 1 and 2 based on parallelized SMA film demonstrator devices and for single SMA film devices. The comparison reveals the potential of upscaling by parallelization. In addition, corresponding values of selected demonstrators for elastocaloric cooling based on fluidic heat transfer are included.*

	f / Hz	$\dot{Q}_0^{cool}/$ mW	$\dot{q}_0^{cool}/$ Wg^{-1}	reference
Parallelized SMA film devices				
Demonstrator 1	0.5	140	0.9	this work
	1	350	2.25	
	2		5.3	
Demonstrator 2	0.25	229	1.19	this work
	0.5	436	2.25	
	1	902	4.67	
Reference SMA film devices				
Single SMA film, compliant design	0.5	20	1.7	[18]
	1	50	4.2	
	2	121	10.3	
	4	222	19	
Antagonistic, concave design	0.5	30	1.9	[10]
	1	64	4.1	
	2	119	7.7	
	4	106	6.8	
Selected demonstrators based on fluidic heat transfer				
Regenerative heat pump	0.25	4536	0.78	[15]
Multistage refrigerator (one stage)	0.125	847	0.77	[12]

The key result of this investigation is the increase of absolute cooling capacity as a consequence of parallelization. At the operation frequency of 1 Hz, the maximum cooling capacity reaches about 900 mW in demonstrator 2. This result compares with the maximum cooling capacity of 220 mW for single SMA film devices, which is observed at 4 Hz reflecting the different heat transfer dynamics. Therefore, we conclude that the cooling capacity scales with the number of active SMA

films, which confirms the advantage in exploiting the concept of parallelization for upscaling (key issue (i)).

The cooling demonstrator is operated in the frequency range up to 2 Hz, which is near the optimum frequency of single SMA film devices. Within the initial 100 s of operation, the demonstrators reach a maximum temperature span of about 3 K between heat sink and source at 1 Hz. This performance is considerably reduced compared to single SMA devices that reach temperature spans up to 14 K [18]. This effect is partly due to the larger thermal mass of heat sink and source. In addition, this performance indicates that heat transfer between parallelized SMA films and heat source/sink elements is less efficient and parasitic heat losses to neighboring components are enhanced (see discussion on reproducibility below). Consequently, investigated demonstrators exhibit a reduced specific cooling capacity in particular at operation frequency above 1 Hz. Therefore, key issue (ii) remains unsolved and further optimization is required to improve heat transfer. Macroscale demonstrators based on fluidic heat transfer generally operate at smaller frequency due to the larger thermal mass of the used SMA wires or tubes and due to experimental restriction in the fluidic circuit. Therefore, their specific cooling capacity is considerably lower compared to thin film devices. Concerning the achieved absolute cooling capacity, the present demonstrators mark a first step and further upscaling will be required to reach performance metrics being comparable to macroscale demonstrators.

The present investigation shows that reproducibility (key issue (iii)) is still a major concern. Compared to single SMA film devices, a lower reproducibility of performance is observed particularly at the heat source to be cooled, where the final temperature varies considerably by about 16 %. This deviation is likely due to the different contact forces at the rather flat profile of the heat source. Despite initial training, plastic deformation takes place during cyclic operation, which may accumulate for each SMA film differently depending on fabrication tolerances. Consequently, non-uniform permanent deformations may occur and thermal contact may decrease for each SMA film differently for increasing cycling time. This effect cannot be compensated on the system level by realignment of the SMA module. In comparison, reproducibility of performance at the heat sink is less critical as the conical profile provides for sufficient contact force.

Reliability of SMA materials (key issue (iv)) is another open point even though considerable progress has been achieved in recent years [26,27]. In particular, optimization of chemical composition allows to meet compatibility criteria of martensitic transformation resulting in ultra-low fatigue performance observed under the ideal conditions of tensile experiments which correlates with hysteresis width [28]. These conditions include the careful sample preparation aiming at a smooth surface finish to minimize functional fatigue. The TiNiFe films investigated in this work do not meet the criteria of ultra-low fatigue. Yet, tensile experiments reveal a typical fatigue life of at least several hundred cycles, which is sufficient for the present investigation of upscaling. However, such fatigue life is hard to achieve under the operation conditions of the investigated demonstrators. Inhomogeneous plastic straining and inhomogeneous stress accumulation may differ among the individual SMA films. Previous work on single film devices showed that inhomogeneities within an individual film could be mitigated, on the material level, by training the SMA films before use and, on the device level, by introducing passive compliant mechanisms to improve mechanical contact for homogeneous loading and to improve thermal contact for efficient heat transfer. These measures turn out to be insufficient for parallel arrangements of SMA film systems. The adjustment of certain operation conditions on the system level like pre-deflection and displacement of the SMA module does not allow for optimization of

the operation conditions of the individual SMA films, which becomes critical at narrow alignment tolerances. A further challenge regarding reliability in parallelized systems is the statistically increased probability of failure. For example, if the failure probability of a single film is 10% in the first 1000 cycles, devices with a single film would have a 90% probability of reaching the 1000 cycles, while this probability reduces to $(0.9)^5 = 59$ % for devices based on five films. Therefore, the durability of the films in parallelized systems is of utmost importance.

7. Conclusions

This paper addresses the topic of upscaling elastocaloric cooling devices based on SMA films, which is a key to establish film-based cooling at length scales beyond the microscale. A new concept of upscaling is proposed that relies on arranging SMA films in parallel in order to increase the overall film mass, while maintaining the large surface-to-volume ratio needed for rapid heat transfer. This approach requires to address several key issues by investigating two demonstrators based on the concept of out-of-plane deflection of SMA films and solid-to-solid heat transfer, which allows for considerable design simplification. The main motivation of this investigation is to increase the cooling capacity. We demonstrate that this issue can be met by parallelization of freestanding SMA films. Demonstrators using five SMA films reach a maximum cooling capacity of about 900 mW compared to a maximum of about 200 mW achieved for single film devices. However, the demonstrators reveal a reduced specific cooling capacity and a reduced temperature span indicating less efficient heat transfer between SMA films arranged in parallel and heat source/sink elements. This issue is strongly interlinked with the drawbacks of reduced reproducibility, which originates from narrow fabrication tolerances causing different plastic straining and inhomogeneous stress accumulation among the individual SMA films. These effects cannot be compensated on the system level, e.g. by realignment of adaptive control of the SMA module. Instead, each SMA film requires dedicated fine tuning of mechanical contact and heat transfer. Therefore, besides improving the reliability at the material level and fabrication accuracy, the next steps for a successful scale-up prototype include novel adaptive designs to allow for individual control of pre-strain and deflection during operation in order to compensate for fabrication tolerances and plastic straining effects.

Conflict of interest
All authors declare no conflicts of interest.

Appendix – Model description

In this work, we built on a two-phase phenomenological model to be regarded as a 3D simplified extension of the original formulation by Tanaka [29]. In Tanaka-type models a macroscale constitutive law linking stress, strain, temperature and phase fraction is coupled with a kinetic law describing the evolution of the phase fraction (treated as an internal variable) as a function of stress and temperature. Here, we assume that the phase fraction of martensite is changing linearly during

the time needed to complete the transformation t_t which is established considering the actual strain rate and transformation strain ε_t (width of pseudoelastic stress plateau).

The model relies on the material parameters and experimentally accessible fit parameters of the TiNiFe films as summarized in Table A 1. Strain-control mode is applied consistent with the tensile test. The transition between elastic regions, governed by Hooke's law, and phase-transformation regions is dictated by the critical stresses, whose increments are computed as a function of the temperature according to the Clausius-Clapeyron relationship:

$$\sigma_{crit}^{\alpha\beta}(T_{sma}) = \sigma_{ref}{}^{\alpha\beta} + c(T_{sma} - T_{ref}) \tag{A1}$$

In Eq. A1, α and β stand for the different phases (martensite and austenite), T_{ref} is the ambient temperature during the test, $\sigma_{ref}{}^{\alpha\beta}$ is the corresponding measured critical stress at the phase transformation onset and $c = d\sigma_{crit}^{\alpha\beta}/dT_{sma}$ is the Clausius-Clapeyron coefficient that describes the linear stress-temperature dependence.

The temperature of the film, T_{sma}, is computed according to the following differential equation, in which both sensible and latent heat transfer are included and which assumes isotropic thermal properties:

$$\rho \cdot c_p \cdot \dot{T_{sma}} = \nabla \cdot (k_x \cdot \nabla T_{sma}) + Q_C + Q_L \tag{A2}$$

In Eq. A2 ρ, c_p and k_x are NiTiFe density, specific heat capacity and thermal conductivity, respectively. The term Q_C represents the losses due to heat conduction while Q_L is a volume heat source introduced to take into account the release/absorption of latent heat during the forward and reverse transformations, calculated as follows:

$$Q_L = \frac{L \cdot \rho}{t_t} \tag{A3}$$

In Eq. A3, L is the latent heat. This expression relies on the simplified assumption that the phase fraction of martensite is increasing/decreasing linearly during the forward and the reverse transformation, respectively. Similarly, the thermal conductivity is set to linearly vary between austenite's and martensite's values.

In terms of thermal boundary conditions, the sample ends are held constant at ambient temperature (Dirichlet condition). This approach is precautionary as it considers the sample fixations as infinite temperature reservoirs (no thermal insulation), which is a penalizing assumption in the context of elastocaloric cooling. Convective heat transfer is assumed to take place on the remaining faces of the film, lengthwise, and at the specified ambient temperature. The amount of heat transferred from each plate face per unit area due to convection is defined as:

$$q_{conv} = h_c \cdot (T_{sma} - T_{amb}) \tag{A4}$$

where h_c is the specified convective heat transfer coefficient and T_{amb} is the ambient temperature. The mechanical and thermal equations are solved by coupled FEM analysis in Matlab.

Table A 1: Material model: thermal, mechanical and process parameters.

MODEL INPUTS				
Parameter	Symbol	Value	Units	Notes or references
THERMAL PARAMETERS				
Austenite thermal conductivity	k_A	18	W/mK	[5,23,30–33]
Martensite thermal conductivity	k_M	8.6	W/mK	[23,31–33]
Specific heat	c_p	450	J/kgK	[5,32]

Latent heat	L	12.3	J/g	Estimation based on experiments and model tuning
Convective heat transfer coefficient	h_c	18	W/(m^2K)	Estimation based on experiments, equal to [5] and comparable to [23,33]
MECHANICAL PARAMETERS				
Austenite's Young modulus	E_A	34.5	GPa	From quasi-isothermal experiment
Martensite's Young modulus	E_M	26.8	GPa	
Poisson's ratio	ν	0.3		[5,23,34]
Density	ρ	6500	kg/m^3	[5,23,32,35–37]
PHASE TRANSFORMATION PARAMETERS				
Clausius-Clapeyron coefficient, forward transformation	c	6.0	MPa/K	Estimation based on experiments, comparable to [23,33,34,38,39]
Critical stress, forward transformation	σ_{crit}^{AM}	419.8	MPa	From quasi-isothermal experiment, taken at plateau midpoints
Critical stress, reverse transformation	σ_{crit}^{MA}	205.6	MPa	
Transformation strain	ε_t	4.10	%	From quasi-isothermal experiment
PROCESS PARAMETERS				
Strain rate	SR	10^{-4}, 10^{-3}, 10^{-2}, 10^{-1}, $3 \cdot 10^{-1}$, 1	s^{-1}	Based on experiments
Holding time	t_{hold}	10	s	
Ambient temperature	T_{amb}	297	K	

References

[1]   S. Fähler, U.K. Rößler, O. Kastner, J. Eckert, G. Eggeler, H. Emmerich, P. Entel, S. Müller, E. Quandt, K. Albe, Caloric effects in ferroic materials: New concepts for cooling, Adv. Eng. Mater. 14 (2012) 10–19. doi:10.1002/adem.201100178.

[2]   W. Goetzler, R. Zogg, J. Young, C. Johnson, Alternatives to vapor-compression HVAC technology, ASHRAE J. 56 (2014) 12–23.

[3]   E. Bonnot, R. Romero, L. Mañosa, E. Vives, A. Planes, Elastocaloric effect associated with the martensitic transition in shape-memory alloys, Phys. Rev. Lett. 100 (2008) 125901.

[4]   S. Qian, Y. Geng, Y. Wang, J. Ling, Y. Hwang, R. Radermacher, I. Takeuchi, J. Cui, A review of elastocaloric cooling: Materials, cycles and system integrations, Elsevier Ltd, 2016. doi:10.1016/j.ijrefrig.2015.12.001.

[5]   H. Ossmer, F. Lambrecht, M. Gültig, C. Chluba, E. Quandt, M. Kohl, Evolution of temperature profiles in TiNi films for elastocaloric cooling, Acta Mater. 81 (2014) 9–20. doi:10.1016/j.actamat.2014.08.006.

[6]   K.F. Hane, T.W. Shield, Microstructure in the cubic to monoclinic transition in titanium-nickel shape memory alloys, Acta Mater. 47 (1999) 2603–2617. doi:10.1016/S1359-6454(99)00143-3.

[7]   R.D. James, K.F. Hane, Martensitic transformations and shape-memory materials, Acta Mater. 48 (2000) 197–222. doi:10.1016/S1359-6454(99)00295-5.

[8]   J. Cui, Y. Wu, J. Muehlbauer, Y. Hwang, R. Radermacher, S. Fackler, M. Wuttig, I. Takeuchi, Demonstration of high efficiency elastocaloric cooling with large Δt using NiTi wires, Appl. Phys. Lett. 101 (2012) 2–6. doi:10.1063/1.4746257.

[9]   G. Ulpiani, G. Ranzi, F. Bruederlin, R. Paolini, F. Fiorito, S. Haddad, M. Kohl, M. Santamouris, Elastocaloric cooling: roadmap towards successful implementation in the built environment, AIMS Mater. Sci. 6 (2019) 1135–1152. doi:10.3934/matersci.2019.6.1135.

[10]   F. Bruederlin, H. Ossmer, F. Wendler, S. Miyazaki, M. Kohl, SMA foil-based elastocaloric cooling: From material behavior to device engineering, J. Phys. D. Appl. Phys. 50 (2017). doi:10.1088/1361-6463/aa87a2.

[11]   S.M. Kirsch, F. Welsch, N. Michaelis, M. Schmidt, A. Wieczorek, J. Frenzel, G. Eggeler, A. Schütze, S. Seelecke, NiTi-Based Elastocaloric Cooling on the Macroscale: From Basic Concepts to Realization, Energy Technol. 6 (2018) 1567–1587. doi:10.1002/ente.201800152.

[12]   R. Snodgrass, D. Erickson, A multistage elastocaloric refrigerator and heat pump with 28 K temperature span, Sci. Rep. 9 (2019) 1–10. doi:10.1038/s41598-019-54411-8.

[13]   F. Welsch, S.-M. Kirsch, N. Michaelis, P. Motzki, A. Schütze, S. Seelecke, Continuous Operating Elastocaloric Heating and Cooling Device: Model-Based Parameter Study With Airflow Losses, in: 2019. doi:10.1115/SMASIS2019-5636.

[14]   S. Qian, A. Alabdulkarem, J. Ling, J. Muehlbauer, Y. Hwang, R. Radermacher, I. Takeuchi, Performance enhancement of a compressive thermoelastic cooling system using multi-objective optimization and novel designs, Int. J. Refrig. 57 (2015) 62–76. doi:10.1016/j.ijrefrig.2015.04.012.

[15]   J. Tušek, K. Engelbrecht, D. Eriksen, S. Dall'Olio, J. Tušek, N. Pryds, A regenerative elastocaloric heat pump, Nat. Energy. 1 (2016) 1–6. doi:10.1038/nenergy.2016.134.

[16]   K. Engelbrecht, J. Tušek, D. Eriksen, T. Lei, C.Y. Lee, J. Tušek, N. Pryds, A regenerative elastocaloric device: Experimental results, J. Phys. D. Appl. Phys. 50 (2017). doi:10.1088/1361-6463/aa8656.

[17]   A. Greco, C. Aprea, A. Maiorino, C. Masselli, A review of the state of the art of solid-state caloric cooling processes at room-temperature before 2019 Point sur l'état de l'art des processus de refroidissement calorique semi-conducteurs à température ambiante avant 2019, Int. J. Refrig. 106 (2019) 66–88. doi:10.1016/j.ijrefrig.2019.06.034.

[18]   F. Bruederlin, L. Bumke, C. Chluba, H. Ossmer, E. Quandt, M. Kohl, Elastocaloric Cooling on the Miniature Scale: A Review on Materials and Device Engineering, Energy Technol. 6 (2018) 1588–1604. doi:10.1002/ente.201800137.

[19]   H. Ossmer, F. Wendler, M. Gueltig, F. Lambrecht, S. Miyazaki, M. Kohl, Energy-efficient miniature-scale heat pumping based on shape memory alloys, Smart Mater. Struct. 25 (2016). doi:10.1088/0964-1726/25/8/085037.

[20]   K. Kim, S. Daly, The effect of texture on stress-induced martensite formation in nickel-titanium, Smart Mater. Struct. 22 (2013). doi:10.1088/0964-1726/22/7/075012.

[21] S. Qian, L. Yuan, J. Yu, G. Yan, The mechanism of Δt variation in coupled heat transfer and phase transformation for elastocaloric materials and its application in materials characterization, Appl. Phys. Lett. 111 (2017). doi:10.1063/1.5001971.

[22] S.M. Kirsch, F. Welsch, N. Michaelis, M. Schmidt, A. Wieczorek, J. Frenzel, G. Eggeler, A. Schütze, S. Seelecke, NiTi-Based Elastocaloric Cooling on the Macroscale: From Basic Concepts to Realization, Energy Technol. 6 (2018) 1567–1587. doi:10.1002/ente.201800152.

[23] F. Wendler, H. Ossmer, C. Chluba, E. Quandt, M. Kohl, Mesoscale simulation of elastocaloric cooling in SMA films, Acta Mater. 136 (2017) 105–117. doi:10.1016/j.actamat.2017.06.044.

[24] H. Ossmer, S. Miyazaki, M. Kohl, Elastocaloric heat pumping using a shape memory alloy foil device, 2015 Transducers - 2015 18th Int. Conf. Solid-State Sensors, Actuators Microsystems, TRANSDUCERS 2015. (2015) 726–729. doi:10.1109/TRANSDUCERS.2015.7181026.

[25] F. Bruederlin, L. Bumke, E. Quandt, M. Kohl, Cascaded SMA-Film Based Elastocaloric Cooling, 2019 20th Int. Conf. Solid-State Sensors, Actuators Microsystems Eurosensors XXXIII, TRANSDUCERS 2019 EUROSENSORS XXXIII. (2019) 1467–1470. doi:10.1109/TRANSDUCERS.2019.8808605.

[26] H. Hou, J. Cui, S. Qian, D. Catalini, Y. Hwang, R. Radermacher, I. Takeuchi, Overcoming Fatigue through Compression for Advanced Elastocaloric Cooling, MRS Bull. 36 (2018) 237. doi:10.1557/mrs.2011.72.

[27] J. Tušek, A. Žerovnik, M. Čebron, M. Brojan, B. Žužek, K. Engelbrecht, A. Cadelli, Elastocaloric effect vs fatigue life: Exploring the durability limits of Ni-Ti plates under pre-strain conditions for elastocaloric cooling, Acta Mater. 150 (2018) 295–307. doi:10.1016/j.actamat.2018.03.032.

[28] C. Chluba, W. Ge, R.L. DeMiranda, J. Strobel, L. Kienle, E. Quandt, M. Wuttig, Ultralow-fatigue shape memory alloy films, Science (80-.). 348 (2015) 1004–1007. doi:10.1126/science.1261164.

[29] K. Tanaka, S. Kobayashi, Y. Sato, Thermomechanics of transformation pseudoelasticity and shape memory effect in alloys, Int. J. Plast. 2 (1986) 59–72.

[30] D.D. Shin, K.P. Mohanchandra, G.P. Carman, High frequency actuation of thin film NiTi, Sensors Actuators, A Phys. 111 (2004) 166–171. doi:10.1016/j.sna.2003.09.026.

[31] A. Coda, M. Urbano, L. Fumagalli, F. Butera, Investigation on the hysteretic behavior of NiTi shape memory wires actuated under quasi-equilibrium and dynamic conditions, J. Mater. Eng. Perform. 18 (2009) 725–728. doi:10.1007/s11665-009-9492-9.

[32] W. Huang, On the selection of shape memory alloys for actuators, (2002) 11–19. doi:10.1016/S0261-3069(01)00039-5.

[33] S. Ahmadi, K. Jacob, F. Wendler, M. Kohl, Shape memory alloy film damping for smart miniature systems, Int. J. Smart Nano Mater. 9 (2018) 199–215. doi:10.1080/19475411.2018.1496953.

[34] K. Ikuta, H. Shimizu, Two dimensional mathematical model of shape memory alloy and intelligent SMA-CAD, IEEE. (1993) 87–92.

[35] C.R. Siviour, J.E. Huber, T. Normanton, N. Petrinic, Strain rate dependence of a super-elastic NiTi alloy, (2009) 1153–1159. doi:10.1051/dymat/2009161.

[36] M. Kök, F. Daʇdelen, A. Aydoʇdu, Y. Aydoʇdu, The change of transformation temperature on NiTi shape memory alloy by pressure and thermal ageing, J. Phys. Conf. Ser. 667 (2016). doi:10.1088/1742-6596/667/1/012011.

[37] P.L. Potapov, E.P. Silva, Time response of Ni-Ti actuator wire, 1 (1995).

[38] J. Tušek, K. Engelbrecht, L. Mañosa, E. Vives, N. Pryds, Understanding the Thermodynamic Properties of the Elastocaloric Effect Through Experimentation and Modelling, Shape Mem. Superelasticity. 2 (2016) 317–329. doi:10.1007/s40830-016-0094-8.

[39] F. Niccoli, Shape Memory Alloy connectors for Ultra High Vacuum applications : a breakthrough for accelerator technologies, 2014.